Investigation of the graphene thermal motion by rainbow scattering

M. Ćosić [a, *], M. Hadžijojić [a], R. Rymzhanov [b, c, d], S. Petrović [a], S. Bellucci [e]

[a] *Laboratory of Physics, Vinča Institute of Nuclear Sciences, University of Belgrade, P. O. Box 522, 11001, Belgrade, Serbia*
[b] *Joint Institute for Nuclear Research, Joliot-Curie 6, 141980, Dubna, Moscow Region, Russia*
[c] *The Institute of Nuclear Physics, Ibragimov St. 1, 050032, Almaty, Kazakhstan*
[d] *L. N. Gumilyov Eurasian National University, Satpayev St. 2, 010008, Astana, Kazakhstan*
[e] *INFN - Laboratori Nazionali di Frascati, 1-00044, Frascati, Rome, Italy*

ARTICLE INFO

ABSTRACT

The thermal motion of graphene atoms was investigated using angular distributions of transmitted protons. The static proton-graphene interaction potential was constructed applying the Doyle-Turner's expression for the proton-carbon interaction potential. The effects of atom thermal motion were incorporated by averaging the static proton-graphene interaction potential over the distribution of atom displacements. The covariance matrix of graphene displacements was modeled according to the Debye theory, and calculated using Molecular Dynamics approach. Proton trajectories were used for construction of angular yields. We have found that there are lines, called rainbows, along which the angular yield is very large. Their evolution in respect to different sample orientation was examined in detail. Further we found that atom thermal motion has negligible influence on rainbows generated by protons experiencing distant collisions with the carbon atoms forming the graphene hexagon. On the other hand, rainbows generated by protons experiencing close collisions with the carbon atoms can be modeled by ellipses whose parameters are very sensitive to the structure of the covariance matrix. Numerical procedure was developed for extraction of the covariance matrix from the corresponding rainbow patterns in the general case, when atoms perform fully anisotropic and correlated motion.

© 2019 Elsevier Ltd. All rights reserved.

1. Introduction

The rainbow effect occurs if particles from neighbouring sections of the impact parameter plane are scattered to the same section of the scattering angle plane. As a consequence, the differential cross-section becomes infinite along certain lines, called rainbows. In 1986, it was predicted that rainbow effect occurs in the classical axial transmission of protons through a very thin Si crystal [1]. The effect, named the crystal rainbow effect, was experimentally verified soon after that [2]. Later, it was shown that the rainbow effect appears also in ion transmission through thicker crystals [3]. Detailed theoretical studies of the rainbows in ion transmission through nanotubes [4] and graphenes [5] have been published.

Transmission of ions through crystals, and nanotubes have large number of potential applications [6—8]. Material analysis plays crucial part in development of new technologies. It has been shown that rainbow scattering could be used for that purpose. Rainbow lines were used for construction of the accurate proton-Si interaction potential [9]. In the case of carbon nanotubes, theoretical studies showed that rainbows could be used for characterization of the nanotube bundles [10,11], determination of the radius and length of the nanotube [12], and for identification of the type and linear density of the aligned Stone-Wales defects [13]. In Ref. [5] it has been suggested that rainbow lines could also be used for determining the Debye-Waller form factor for atoms in the graphene and other similar materials.

Nowadays existing and emerging nanotechnologies try to harness exceptional properties of various nanostructured materials such as very thin crystals, nanotubes or graphene. Some of exotic graphene thermal properties are extremely high thermal conductivity [14], and a large near-field radiative heat transfer [15] which can be several order of magnitude larger than limit set by the Stefan-Boltzmann law. Many of the thermal properties of graphene are shared with graphite and stem out of its anisotropy [16]. The lattice vibrations (phonons) determine the specific heat of graphene [17,18]. The peculiar thermal properties of graphene can be connected with corresponding specific lattice vibrations [19]. The

---

* Corresponding author.
E-mail address: mcosic@vinca.rs (M. Ćosić).

result varies for free-standing graphene compared to graphene on different substrates. The analysis of graphene's thermal vibrations can be full of far-reaching consequences even for the realization of devices where the thermal properties of graphene can play a role.

Thermally induced motion of atoms in graphene is highly nontrivial. For example, according to the famous and experimentally verified Mermin-Wagner theorem [20] atom thermal fluctuations destroy any long range crystalline ordering at any finite temperature. The conclusion, which held for more than 30 years, was that perfect planar crystal can't exist. This was one of the main reasons why discovery of graphene immediately induced such scientific interest. Later, detailed investigations showed that interaction between bending and stretching can stabilise graphene sheet, but as a consequence graphene sheet becomes rippled [21]. Thus perfect 2D crystal can exist but only in the 3D space. Although finite, fluctuations of the graphene ripples hight can be very large as predicted in Molecular dynamics simulations [22]. Another way to circumvent the restrictions of the Mermin-Wagner theorem, reported in the Ref. [23], is to assume that flat shape of graphene arises due to buckling of the atoms on the smallest possible scale which results in up–down asymmetry of the graphene. It is clear that thermal motion of atoms in this two cases can be very different.

In this paper we will elaborate on the idea stated in the Ref. [5] that rainbow scattering of 5-keV protons could be used for investigation of the thermal motion of graphene atoms. Covariance matrix of atom displacements will be modeled according the Debye theory, and calculated using Molecular Dynamics approach. It should be noted that set of all positive definite matrices can be decomposed into equivalence classes consisting of rotationally equivalent matrices. Thus, arbitrary covariance matrix can be classified according the number of distinct eigenvalues in its spectrum. It will be shown that rainbow scattering allows one to distinguish between covariance matrices belonging to the different classes. Therefore, our analysis applies to the most general case possible of the carbon atom thermal motion.

The plan of the paper is as follows. In sec. 2 we develop the theoretical framework, constructing firstly the interaction potential, and then finding the solutions of the equations of motion for proton scattering by the graphene. Obtained trajectories will be then used for the construction of the mapping of the impact parameter plane to the transmitted angle plane allowing us to describe the proton-graphene rainbow structure. In sec. 3 we discuss in detail our results, determining firstly the covariance matrix of the graphene vibrations, and then proceeding to describe the transmission rainbow patterns, before showing finally how to extract the covariance matrix from the rainbow patterns in the general case when atoms perform fully anisotropic and correlated motion. We draw the conclusions of our work in the last section, *i.e.* sec. 4.

2. Theory

2.1. Construction of interaction potential

In this chapter it was adopted that median plane of the graphene coincides with the transverse plane *xOy* of the Cartesian coordinate reference system, which *z* axis points in the direction of the proton transmission. In this convention *x* is the vertical while *y* is the horizontal axis. In respect to this coordinate system the direction of the proton beam was specified by polar angle Θ and azimuthal angle Φ (measured in respect to the positive direction of the *y* axis), respectively.

We have assumed that proton-carbon interaction potential energy is adequately described by the Doyle-Turner's expression [24].

$$V(\boldsymbol{\rho}) = \frac{Z_1 \hbar^2}{4\sqrt{\pi} m_o} \sum_{k=1}^{4} \frac{\alpha_k}{\sqrt{\left|\det \frac{\beta_k}{16\pi^2} \boldsymbol{I}\right|}} \exp\left[-\frac{1}{4}\boldsymbol{\rho}^T \cdot \left(\frac{\beta_k}{16\pi^2}\boldsymbol{I}\right)^{-1} \cdot \boldsymbol{\rho}\right],$$

(1)

where $\boldsymbol{\rho}$ is a column vector of proton-carbon relative distance, $\boldsymbol{\rho}^T$ denotes transposed distance vector, $\boldsymbol{I}$ is identity matrix; $\boldsymbol{\alpha} = (0.07307, \ 0.1951, \ 0.04563, \ 0.01247)$ nm and $\boldsymbol{\beta} = (0.369951, 0.112966, 0.028139, 0.003456)$ nm^2 are carbon Doyle-Turner fitting parameters [24]; $\hbar$ is the reduced Planck constant, m_o is electron mass, and $Z_1 = 1$ is proton atomic number.

The interaction time of protons having kinetic energy $E_k = 5$ keV with individual carbon atoms is considerable shorter than period of the atom thermal vibrations. Therefore, transmitting through graphene sheet the proton effectively interacts with the static lattice in which atoms are randomly displaced from the equilibrium position [25,26]. Strictly speaking thermal motion brakes the symmetry of the graphene sheet. However, since amplitude of vibrations statistically fluctuate the effect of translational symmetry braking is small, and shall be neglected. Rotational symmetry of graphene potential will remain broken since in graphene amplitude of off-plane displacements can be significantly different from the corresponding amplitudes of in-plane displacements. The simplest way to introduce thermal vibrations while respecting the graphene translational symmetry is to model the effective potential at a given distance from the atom equilibrium position as an average potential of fictitious ensemble consisting of the large number of displaced carbon atoms. Let vector $\boldsymbol{\rho}$ represents the distance of the proton from the atom equilibrium position and $\boldsymbol{\rho}_n$ the displacement vector of the *n*-th atoms. The ensemble averaged potential is then given by the equation

$$V_{th}(\boldsymbol{\rho}) = \frac{1}{N} \sum_{n=1}^{N} V(\boldsymbol{\rho} - \boldsymbol{\rho}_n),$$

(2)

where *N* represents the total number of atoms. Note that vectors $\boldsymbol{\rho}_n$ for $n = 1, ..., N$ are random samples from the probability distributions P_n^{th} of individual atoms which in principle can be different (because of boundary conditions, presence of defects *etc.*), thus the introduced virtual copies of atom do not represent the statistical ensemble.

When number of atoms in a graphene *N* is large the Eq. (2) can be further simplified. The arithmetic average in Eq. (2) removes explicit dependence on the carbon atom displacements making every lattice site again equivalent. Following the same logic let us introduce the concept of "averaged atom", whose physical properties are the arithmetic averages of the individual atom properties. Displacement of such atom is given by the expression

$$\boldsymbol{\rho}^{'} = \frac{1}{N}(\boldsymbol{\rho}_1 + ... + \boldsymbol{\rho}_N)$$

(3)

Since atoms differ only by the way they vibrate, averaging do not affect other physical properties. We shall replace each member of the introduced ensemble by averaged atom, and create new ensemble of identical copies *i.e* the statistical ensemble. Average displacement vector $\boldsymbol{\rho}^{'}$ now should be interpreted as a new random variable with probability distribution P_{th}, whose different samples now characterize different states of the atoms forming the statistical ensemble. According the central limit theorem [27], when $N \rightarrow \infty$ the probability distribution P_{th} becomes the multivariate normal distribution [28] given by the following expression

$$P_{th}\left(\boldsymbol{\rho}'\right) = \frac{1}{\sqrt{(2\pi)^3|\det\boldsymbol{\Sigma}|}}\exp\left[-\frac{1}{2}\boldsymbol{\rho}'^T\cdot\boldsymbol{\Sigma}^{-1}\cdot\boldsymbol{\rho}'\right],\tag{4}$$

where $\boldsymbol{\Sigma} = \mathscr{E}(\boldsymbol{\rho}'\cdot\boldsymbol{\rho}'^T)$ is a covariance matrix defined as a mathematical expectation of the matrix $\boldsymbol{\rho}'\cdot\boldsymbol{\rho}'^T$. The potential V_{th} now can be expressed as an ensemble average over the distribution P_{th}

$$V_{th}(\boldsymbol{\rho}) = \lim_{N\to\infty}\frac{1}{N}\sum_{n=1}^{N}V(\boldsymbol{\rho}-\boldsymbol{\rho}_n) \approx \int_{\boldsymbol{\rho}'}V\left(\boldsymbol{\rho}-\boldsymbol{\rho}'\right)P_{th}\left(\boldsymbol{\rho}'\right)\mathrm{d}^3\boldsymbol{\rho}',\tag{5}$$

which can be evaluated analytically giving

$$V_{th}(\boldsymbol{\rho}) = \frac{Z_1\hbar^2}{4\sqrt{\pi}m_o}\sum_{k=1}^{4}\frac{\alpha_k}{\sqrt{\left|\det\left(\frac{\beta_k}{16\pi^2}\boldsymbol{I}+\frac{1}{2}\boldsymbol{\Sigma}\right)\right|}}$$
$$\times\exp\left[-\frac{1}{4}\boldsymbol{\rho}^T\cdot\left(\frac{\beta_k}{16\pi^2}\boldsymbol{I}+\frac{1}{2}\boldsymbol{\Sigma}\right)^{-1}\cdot\boldsymbol{\rho}\right].\tag{6}$$

The proton-graphene interaction potential is the sum of proton-carbon interaction potentials that dominantly contribute to the scattering process. Since all thermally averaged proton-graphene potentials are now equal, introduced sum should reflect graphene translational symmetry and geometric structure. The rhombic Bravais lattice of graphene is defined by the primitive vectors $\boldsymbol{a}_1 = (\sqrt{3}l/2, 3l/2, 0)$ and $\boldsymbol{a}_2 = (-\sqrt{3}l/2, 3l/2, 0)$, where $l = 0.144$ nm is the carbon-carbon bond length. The repeating motif consists of two carbon atoms. Positions of the left and the right atom respectively, relative to the vertices of the unit cells are $\boldsymbol{g}_1 = (0, -l/2, 0)$ and $\boldsymbol{g}_2 = (0, l/2, 0)$. In the coordinate system attached to the center of the graphene unit cell positions of the carbon atoms in graphene are given by the following equation

$$\boldsymbol{R}_{n_1,n_2,n_3} = \frac{1}{2}(2n_1-1)\boldsymbol{a}_1 + \frac{1}{2}(2n_2-1)\boldsymbol{a}_2 + \boldsymbol{g}_{n_3},\tag{7}$$

where n_1 and n_2 are integers, and $n_3 = 1, 2$. The potential at the point $\boldsymbol{r}$ relative to the unit cell center reads

$$U(\boldsymbol{r}) = \sum_{n_1,n_2}\sum_{n_3=1}^{2}V_{th}\left(\boldsymbol{r}-\boldsymbol{R}_{n_1,n_2,n_3}\right).\tag{8}$$

2.2. The proton-graphene rainbow scattering

Newton equations of motion for protons scattering by the graphene sheet read

$$m\frac{d}{dt}\boldsymbol{v} = -\nabla U(\boldsymbol{r})\tag{9}$$

where m stands for the proton mass, $\boldsymbol{v}$ for its velocity vector, and t denotes the time. The angular deflection with respect to the z axis, is described by the pair of angles $\boldsymbol{\theta} = (\theta_x, \theta_y)$, defined by the expressions: $\tan\theta_x = v_x/v_z$, and $\tan\theta_y = v_y/v_z$, respectively. The angular proton yield in the plane $z = z_0$, labeled $Y_\theta(\boldsymbol{\theta}; z_0)$ is defined as the number of protons in the surface element $d\theta_x d\theta_y$ centered at the angle $\boldsymbol{\theta} = (\theta_x, \theta_y)$. Potential $U(\boldsymbol{r})$ has non-negligible values only for $-z_m \leq z \leq z_m$ called the interaction interval, planes $z = -z_m$, and $z = z_m$ are called the entrance and the exit plane respectively. This means that shapes of distribution $Y_\theta(\boldsymbol{\theta}; z_0)$ can change only for variable z_0 in the interaction interval, thus yield $Y_\theta(\boldsymbol{\theta}; z_0)$ recorded by the detector placed far away ($z_0 \to \infty$) is actually equal to the

$Y_\theta(\boldsymbol{\theta}; z_m)$.

We have assumed that the proton beam is parallel, monochromatic of kinetic energy E_k, and uniformly distributed in the initial transverse plane. Therefore, appropriate initial conditions at the entrance plane are $\boldsymbol{r}(0) = (\boldsymbol{b}, -z_m)$ and $\boldsymbol{v}(0) = v(\sin\Theta\cos\Phi, \sin\Theta\sin\Phi, \cos\Theta)$, respectively, where proton impact parameter vectors $\boldsymbol{b} = (b_x, b_y)$ are samples from the uniform distribution and v is their initial velocity $v = \sqrt{2E_k/m}$.

Solutions of Eq. (9) for all $\boldsymbol{b}$ define a mapping $\boldsymbol{\theta}(\boldsymbol{b}; \Theta, \Phi)$ of initial positions in the entrance plane to the final deflection angles $\boldsymbol{\theta}$ in the exit plane, angles Θ and Φ are treated as fixed parameters. It can be shown that differential cross-section in the exit plane $\sigma_{\mathrm{diff}}(\boldsymbol{\theta}; \Theta, \Phi)$ is proportional to the ratio of infinitesimal surface elements $db_x db_y/d\theta_x d\theta_y$. Using the introduced mapping $\boldsymbol{b} \to \boldsymbol{\theta}$ the differential cross-section in the entrance plane can be expressed as [5].

$$\sigma_{\mathrm{diff}}(\boldsymbol{b}; \Theta, \Phi) \sim \frac{1}{|\det\boldsymbol{J}_\theta(\boldsymbol{b}; \Theta, \Phi)|},\tag{10}$$

where $\boldsymbol{J}_\theta(\boldsymbol{b}; \Theta, \Phi)$ is Jacobian matrix of the mapping $\boldsymbol{b} \to \boldsymbol{\theta}$. Note that Jacobian is singular along the lines which are solutions of the equation

$$|\det\boldsymbol{J}_\theta(\boldsymbol{b}; \Theta, \Phi)| = 0,\tag{11}$$

which are called the impact parameter rainbows lines. In the exit plane the differential cross-section $\sigma_{\mathrm{diff}}(\boldsymbol{\theta}; \Theta, \Phi)$ is infinite along the lines, called angular rainbow lines, which are images of the impact parameter rainbow lines. According to the inverse function theorem, angular rainbows separate areas of different multiplicity of the mapping $\boldsymbol{\theta} \to \boldsymbol{b}$ (i.e. mapping inverse to the $\boldsymbol{b} \to \boldsymbol{\theta}$). The area of larger multiplicity is called the bright side of the rainbow while the area of lower multiplicity is called the dark side of the rainbow. Therefore, singularities and multiplicity of the mapping $\boldsymbol{\theta} \to \boldsymbol{b}$ dominantly determine the shape of angular distributions $Y_\theta(\boldsymbol{\theta}, z_m)$.

3. Results and discussion

We assume that the graphene samples are produced following similar procedures as described in Refs. [21,29]. In the first approach graphene sheet is epitaxially grown on appropriate substrate. Substrate was then removed, and cleaned graphene sheet transferred to a high quality TEM grid which provides mechanical support and allows proton transmission only through grid openings. The size of the grid was assumed to be sufficiently large that obtained graphene sample can be considered as freestanding infinite graphene sheet [29]. In the second approach on-top of a epitaxially grown graphene metallic scaffolding of decreasing spacing was deposited. Substrate was removed only form parts of the sample leading to the collection of the suspended graphene nanoribbons [21].

In this paper we study interaction of a uniform 5-keV proton micro beam [30] with described graphene samples. Schematics diagram of the appropriate experimental setup is shown in Fig. 1. It consists of: a proton source, an accelerator system, collimation system and an interaction chamber equipped with the 3-axis goniometer and detector. Proton detection system consists of angularly resolved electrostatic analyzer, and image sensor [31–34]. Construction of its electrodes prevents detection of the neutral particles, while at the same time alow detection of protons belonging to the specific scattering plane (set by the azimuthal angle of goniometer) and of specific energy (set by the electrode voltage). The detected proton position is directly proportional to the scattering angle. We assume that the angular and energy resolution of the detector are approximately 1 mrad and 0.15%
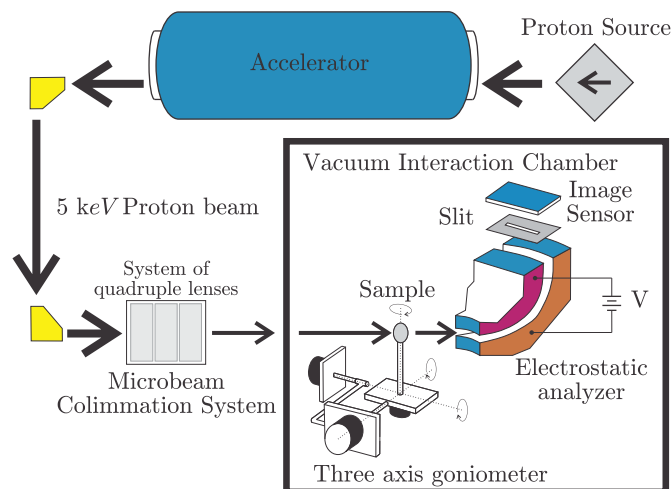
Fig. 1. Schematics of the experimental setup. (A colour version of this figure can be viewed online.)

respectively. It has been shown that small angular and energy dispersions of the proton beam have negligible effect on the rainbow patterns. They influence only the sharpness of the rainbow light-to-dark transitions [5]. Moreover, both dispersions are small for the micro beam and will be neglected [30].

Proton de Broglie wavelength $\lambda = 4.0476 \times 10^{-4}$ nm is considerable smaller than the carbon-carbon bond length $l = 0.144$ nm, therefore protons can be treated as classical particles. It has been shown that for protons in this energy range the Ziegler-Biersack-Littmark theory of energy loss gives results of acceptable accuracy [35,36]. According to it total proton energy loss and dispersion of the scattering angle caused by interaction with electrons are equal to 22 eV and 0.35 mrad respectively. Both values are smaller than analyzer resolutions and will be neglected. The probability for neutralization of 5-keV protons is around 40%, while probability for multiple ionization processes is negligible [35,36]. Therefore, electrostatic analyzer should be set in such way to enable detection only of particles having exit charge state +1, and energy of 5-keV. The pressure in the interaction chamber should be approximately 5×10^{-9} mbar in order to minimize contamination of the sample and deformation of proton beam before and after interaction with the target. High vacuum is important for correct operation of the electrostatic analyzer, since it minimizes distortion of the electric field of its electrodes, and increases measurable energy range.

Real samples are rarely perfect. Usually they are contaminated by impurities, leftovers from the production processes, and can contain defects of various kind. Mechanisms of defect formation in nano-structured materials are significantly different than those producing defects in bulk solids [37], and interaction with the substrate can influence the defect formation [38]. It is interesting to note that presence of defects does not necessarily have negative effect on the properties of nano-structured martials. Ion beam can be used for inducing controllable changes of material morphology, and for fine tuning of their mechanical, electric, and magnetic properties [7,38–41]. However, in this case special care must be taken to minimize the damage of the graphene samples caused by the proton beam. The energy required to displace carbon atom from graphene sheet is around $E_d = 22.2$ eV [42]. Proton creates vacancy in direct head-on collision only if its kinetic energy is larger than threshold of approximately $E_{min} = (1 + \xi)^2/(4\xi)E_d = 78.2$ eV, where $\xi \approx 12$ is the ratio of proton and carbon masses [42]. Any proton is potentially capable of producing defects. However, according to the ZBL theory for 5-keV protons electronic energy loss is

approximately 35 times larger than nuclear energy loss. On average out of 22eV lost in proton transmission through graphene sheet, only 0.63 eV is transferred to the motion of carbon atoms. Therefore we can conclude that probability for the single defect formation is low, and that probability for double vacancy or complex defect formation is negligible (see also Fig. 1. (c), (d), and (f) of the Ref. [42]). This conclusion is confirmed by the SRIM calculation which predicts formation of 0.0023 vacancies per proton impact. Therefore, if applied proton fluence is low enough (approximately 10^{12}–10^{13} protons per cm^2) then defect formation is minimized. Lower operating proton current also improves operation of proton detector since it prevents saturation of the image sensor.

3.1. The covariance matrix

To model the covariance matrix Σ of the graphene steady state thermal motion we have considered two different approaches. In the first approach we have assumed that thermal vibrations of the carbon atoms are isotropic and adequately described by the Debye model [25,26,43]. The covariance matrix is then $\Sigma = \sigma I$, probability density distribution of atom displacements is

$$P_{th}(\boldsymbol{\rho}') = \frac{1}{(2\pi\sigma^2)^{3/2}} \exp\left[-\frac{\|\boldsymbol{\rho}'\|^2}{2\sigma^2}\right], \tag{12}$$

and variance of displacements is

$$\sigma^2 = \frac{3\hbar^2}{M_c m_u k_B \Theta_D} \left(\frac{\mathfrak{D}_f(\Theta_D/T)}{\Theta_D/T} + \frac{1}{4}\right), \tag{13}$$

here $M_c = 12.0107$ is carbon atomic weight, $m_u = 1.6605 \cdot 10^{-27}$ kg is universal atomic mass unit, $\Theta_D = 2000$ K is the carbon Debye temperature of diamond [25], $k_B = 1.3806 \cdot 10^{-23}$ J/K is Stefan-Boltzmann's constant, T is the graphene absolute temperature, and $\mathfrak{D}_f$ is the Debye's function. At the temperature $T = 300$ K, according to Eq. (13), variance of the carbon atoms displacements is $\sigma = 17.3663$ pm^2.

This simple model correctly describes thermal vibration of atoms forming cubic crystals [25,26], or carbon nanotubes [44]. In the case of freestanding graphene, or nanoribbons, Debye model is applicable only for very low temperatures. Because there is no stabilizing influence of the neighbouring layers, variance of the off-plane displacements should be larger than variances of the in-plane displacements. Therefore, in the second approach the correct atom displacements were calculated using Lammps a classical molecular dynamic simulator [45].

Atom trajectories were calculated by taking into account contributions from all neighbouring atoms filling a rhombic prism. The size of computational supercell is $N_1 \boldsymbol{a}_1 \times N_2 \boldsymbol{a}_2 \times c\boldsymbol{e_z}$, where N_1, N_2, and c denote numbers of unit cells in directions of primitive vectors, and its size in the normal direction, respectively. To eliminate influence of the artificial boundary in the normal direction a very large value was chosen for the parameter $c = 4$ nm. The interatomic force was calculated from Airebo-type potential with parameterization taken from the Ref. [46]. All simulations were performed within the canonical phase space distribution corresponding to the constant volume, temperature and number of particles (the NVT ensemble). A time step of 1 fs was used in calculations and the state of the supercell was saved in each time step for subsequential analysis.

We will illustrate the procedure for calculation of the covariance matrix in the case of graphene sheet. Let us define the time dependent covariance matrix of the n-th atom displacements $\Sigma_n(t)$ by the relation

$$\Sigma_n(t) = \frac{1}{\tau} \int\limits_{t-\tau/2}^{t+\tau/2} \begin{bmatrix} x_n^2(t'), & x_n(t')y_n(t'), & x_n(t')z_n(t') \\ y_n(t')x_n(t'), & y_n^2(t'), & y_n(t')z_n(t') \\ z_n(t')x_n(t'), & z_n(t')y_n(t'), & z_n^2(t') \end{bmatrix} dt' \tag{14}$$

When t is large, integral in the Eq. (14) is dominated by the steady state motion of the carbon atom. Therefore, the covariance matrix of the n-th atom displacements is $\Sigma_n = \lim_{t\to\infty}\Sigma_n(t)$. Note also that length of the fixed time interval τ, called window, must be sufficiently large so that steady state motion can be accurately represented. According to the central limit theorem time dependent covariance matrix $\Sigma(t)$, and covariance matrix of the graphene steady state motion Σ are given by following expressions

$$\Sigma = \lim_{t\to\infty}\Sigma(t) = \lim_{t\to\infty}\frac{1}{N}\sum_n \Sigma_n(t) = \frac{1}{N}\sum_n \Sigma_n, \tag{15}$$

where $N = 2N_1N_2$ is number of atoms.

In the case of graphene sheet, periodic boundary conditions were applied in the plane, while fixed boundary conditions were applied in the normal direction.

Fig. 2 shows calculated results for supercell containing $N = 11250$ atoms (*i.e.* 75 × 75 unit cells) at the temperature of $T =$ 300 K. Averaged displacements squared in x, and z directions, respectively, are shown in the Fig. 2(a) by gray lines. Graph of the averaged displacement squared in the y direction looks almost completely identical to the graph of the corresponding displacement in the x direction and it is not reproduced here. Fig. 2(a) clearly reveals that the settling time of the graphene transient response is approximately 2 ns.

Red lines in Fig. 2(a) show xx and zz components of the matrix $\Sigma(t)$ (*i.e.* functions $\sigma_x^2(t)$, and $\sigma_z^2(t)$). We have found that optimal window size was $\tau = 2$ ns. The remaining diagonal component $\sigma_y^2(t)$ was found to be practically indistinguishable from the $\sigma_x^2(t)$, and is not shown here. Values of off-diagonal components of the matrix $\Sigma(t)$ were found to be small irregularly fluctuating around 0 pm². Maximal deviation from the mean value of approximately 0.8 pm² was observed for xz and yz matrix components.

In order to estimate the $t\to\infty$ limit the first 2 ns representing transient responses of the matrix $\Sigma(t)$ was discarded. Remaining parts were fitted by the function $A + B\exp(-Ct)$, which allows easy determination of the $t\to\infty$ limit. If resulting value of the exponent C is very large then fitting procedure can be numerically unstable. In that case covariance matrix components were fitted by the constant function. Obtained fitting function for xx and zz matrix components are in Fig. 2(a) shown by the blue lines.

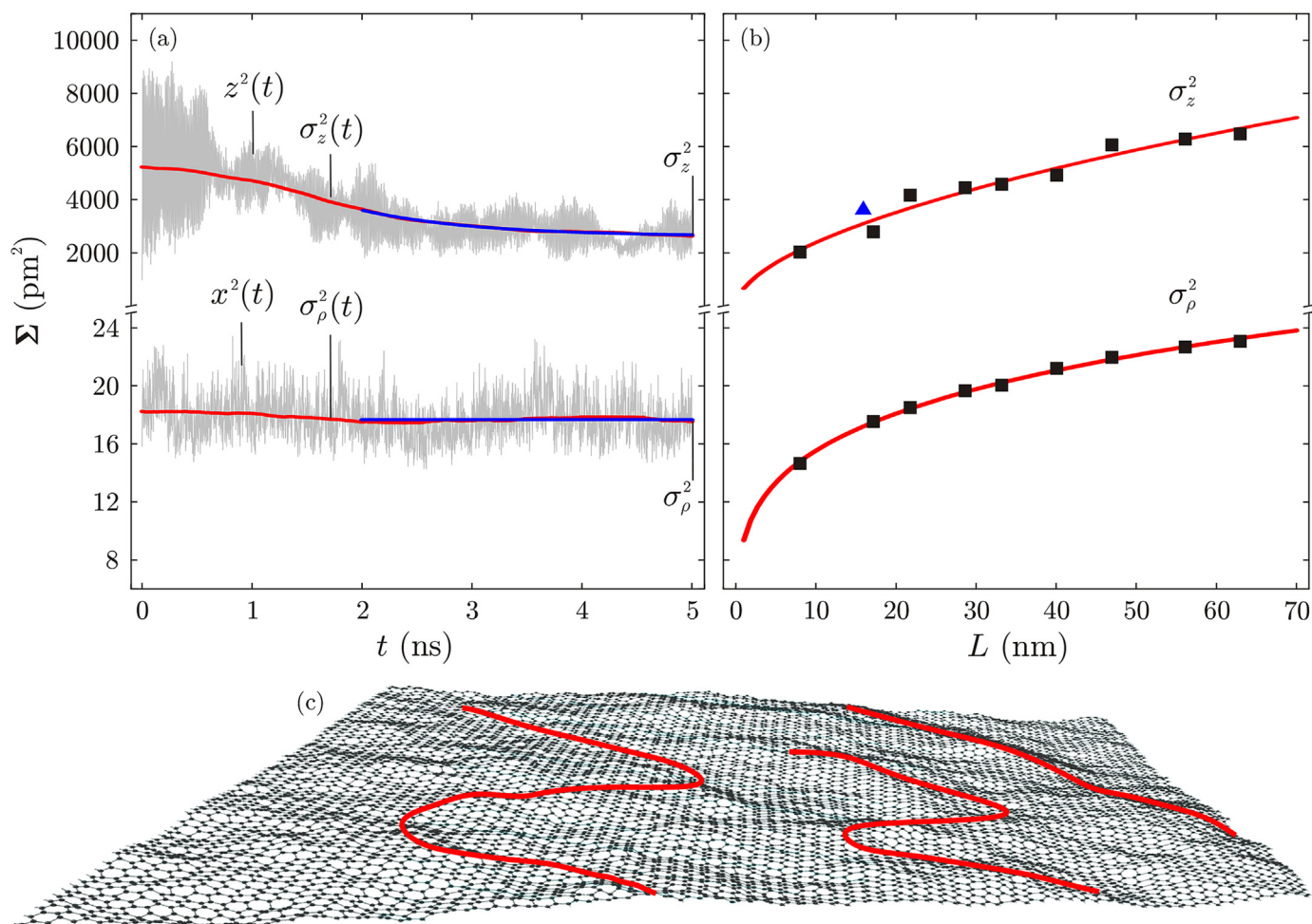We have found that magnitudes off-diagonal elements of the

Fig. 2. (a) Dependencies of the atom mean squared displacements (the gray lines), and covariance matrix components (the red lines) on time for graphene at $T = 300$ K. The blue lines show fits of covariance matrix components only for the atom steady state motion. (b) Solid black squares show scaling of the equilibrium covariance matrix components with the linear supercell size L, red lines are fits by the power law AL^ζ. Solid blue triangle shows the result of the simulation from the Ref. [22]. (c) State of the graphene sheet at $t = 2.9$ ns. Major ripples are denoted by thick red lines. (A colour version of this figure can be viewed online.)

matrix Σ are more than 80 times smaller than magnitudes of diagonal components. They were neglected in subsequent analysis. It should be noted that difference $\sigma_y^2 - \sigma_x^2$ was found to be two times smaller than magnitude of the smallest neglected component σ_{xy}. Therefore, we have disregarded this difference, defined the quantity $\sigma_\rho^2 = (\sigma_x^2 + \sigma_y^2)/2$, and took that matrix $\Sigma = \text{diag}(\sigma_\rho^2, \sigma_\rho^2, \sigma_z^2)$ $= \text{diag}(17.67, 17.67, 2619.10)$ pm^2 represents the true covariance matrix of the graphene thermal vibrations, at the $T = 300$ K. The final result is in agreement with the graphene symmetry which requires that in the steady state atoms perform uncorrelated, and isotropic in-plane motion. All obtained results are summarized in the Table 1. Described procedure was subsequently applied for determination of all considered covariance matrices.

Note that components of the Σ are finite in contrast to the claims of the Mermin-Wagner theorem [20] which implies that they should be infinite. Our calculations show that the same conclusion holds for other temperatures. Obviously, higher order interactions such as many-body interaction which are neglected in the Ref. [20], but included in the AIREBO potential [46], are responsible for the stabilization of the graphene. However, this doesn't mean that variance of the off-plane motion can't be very large. Similar behaviour was noticed long time ago in the theoretical calculation of the off-plane variance of a single graphite sheet [47]. It has been shown that it is essential to include the shear interaction between neighbouring graphite layers in order to get a good agreement with the experiment.

To really understand nature of graphene motion we have investigated the scaling of the matrix Σ with increased linear sample size L defined by the following relation $L = \sqrt{L_x L_y}$, where L_x, and L_y are sizes of the sample in the x, y direction, respectively. We have analysed supercells containing $N = 2450, 11250, 18050, 31250, 42050, 61250, 80000, 84050$, and 120050 carbon atoms. In Fig. 2(b) those 18 data points are shown by the solid black squares. The data show that both variances σ_z^2 and σ_ρ^2 are increasing with the size of the sample. Obtained results were fitted by the power law AL^ζ suggested by the phenomenological theory of thermal fluctuations in flexible membranes [48]. Resulting fits are in Fig. 2(b) shown by the red lines. On the other hand, positions of peaks in the radial distance distribution function were found to match with the corresponding peaks for the perfect static lattice, implying that samples retain their crystalline ordering. Both this facts are implying that graphene sheet became rippled, as can be seen from Fig. 2(c) which shows the state of the supercell, containing 11250 atoms, at $t = 2.9$ ns. This figure shows that graphene "landscape" is dominated by three major ripples marked by the red lines.

The accuracy of obtained result was checked by comparison with the results of Monte-Carlo calculations [22] and with experimental data [49]. Data point reported in the Ref. [22] is shown in Fig. 2(b) by the solid blue triangle. The variance of the planar vibrations $\sigma_\rho^2 = 17.67$pm^2, is in good agreement with the prediction of the Debye model ($\sigma = 17.37$pm^2), and with the experimental data (15.2 pm^2). Variance of vibrations in the normal direction $\sigma_z^2 =$

2619.10 pm^2 is in good agreement with the value reported in the Ref. [22] ($\sigma_z^2 = 3600$ pm^2). However, both theoretical values are considerable larger than the corresponding experimental value (104 pm^2).

This large discrepancy can be explained by two factors. We have found that results of the our Molecular Dynamics simulations are highly sensitive to the even smallest amount of strain. For example, shrinking of the computational supercell by 0.4%, due to the compressive strain in the y direction, leads to the increase of the σ_z^2, of more than 13 times. On the other hand, the same amount of expansive strain decreases σ_z^2 only by a factor 1.14, while expansion of the supercell by 0.5% in both directions decreases σ_z^2 by a factor of 2.08. Therefore, we argue that the large observed difference can be partly explained by the presence of the expansive strain between graphene and the substrate. Secondly, authors of the Ref. [49] themselves claim that at temperatures smaller than $T \leq 800$ K there is a significant presence of the surface contaminants which suppress atom off-plane motion while disturb only slightly their in-plane motion.

In the case of the nanoribbons the covariance matrix Σ was calculated following the procedure outlined in the previous paragraphs, with a few minor modifications. As already described at the beginning of this section the second sample contains nanoribons suspended over the bars of the metallic ladders. Let us assume that bars are vertical. Nanoribbon then extends in the x direction, while its atoms are free to move in the y direction. We also assume that bars strongly suppress the motion of the carbon atoms interacting with them. Therefore, computational supercell have form of the rectangular prism of size $\sqrt{3}N_1 l e_x \times 3N_2 l e_y \times c e_z$, which consists of N_1, and N_2 unit cells in the x, and y directions, respectively. Hight of the unit cell $c = 4$ nm was the same as in previous calculations. Appropriate boundary conditions are combination of periodic with frozen boundary atoms in x direction, free boundary condition in the y direction, and fixed boundary conditions in the direction normal to the ribbon. We have found that steady state covariance matrix have form $\Sigma = \text{diag}(\sigma_x^2, \sigma_y^2, \sigma_z^2) = \text{diag}(18.14, 35.45, 3698.18)$ pm^2. Double degeneracy of the eigenvalue σ_ρ^2 is now lifted indicating that carbon atoms now perform fully anisotropic uncorrelated motion, which also leads to the rippling of the nanoribbon. Summary of all obtained results can be found also in the Table 1.

3.2. The transmission rainbow patterns

It has been shown that in general graphene rainbow pattern consist of two parts. The outer lines formed by protons experiencing close encounters with graphene carbon atoms, and the inner lines formed by protons collectively scattered by the graphene hexagons [5]. The inner rainbows, which give information of the graphene structure, were studied extensively in the Ref. [5]. In present paper main focus is on the outer rainbow pattern.

All rainbows will be shown in the transverse plane of the coordinate system attached to the proton beam. It will be shown that, in this coordinate system, relevant rainbow lines have an elliptical shape which behaves, in a qualitatively equivalent manner as a projection of the bilinear form associated with the matrix Σ^{-1}. Angular distributions were constructed from 1 517 282 proton trajectories which impact parameters uniformly cover the impact parameter plane.

Figure 3 shows obtained rainbow lines together with corresponding distribution in the case of isotropic thermal vibrations ($\sigma = 17.37$ pm^2) for normal incidence Fig. 3(a), sample tilted by an angle $\Theta = 0.065\pi$ rad Fig. 3(b), and sample additionally rotated by an angle $\Phi = 0.25\pi$ rad Fig. 3(c). Enlarged views of the central parts of presented images are shown in the corresponding insets in the

Table 1
: Equilibrium values of components of covariance matrix Σ, obtained by fitting procedure. Error terms are standard errors of the fitting procedure.

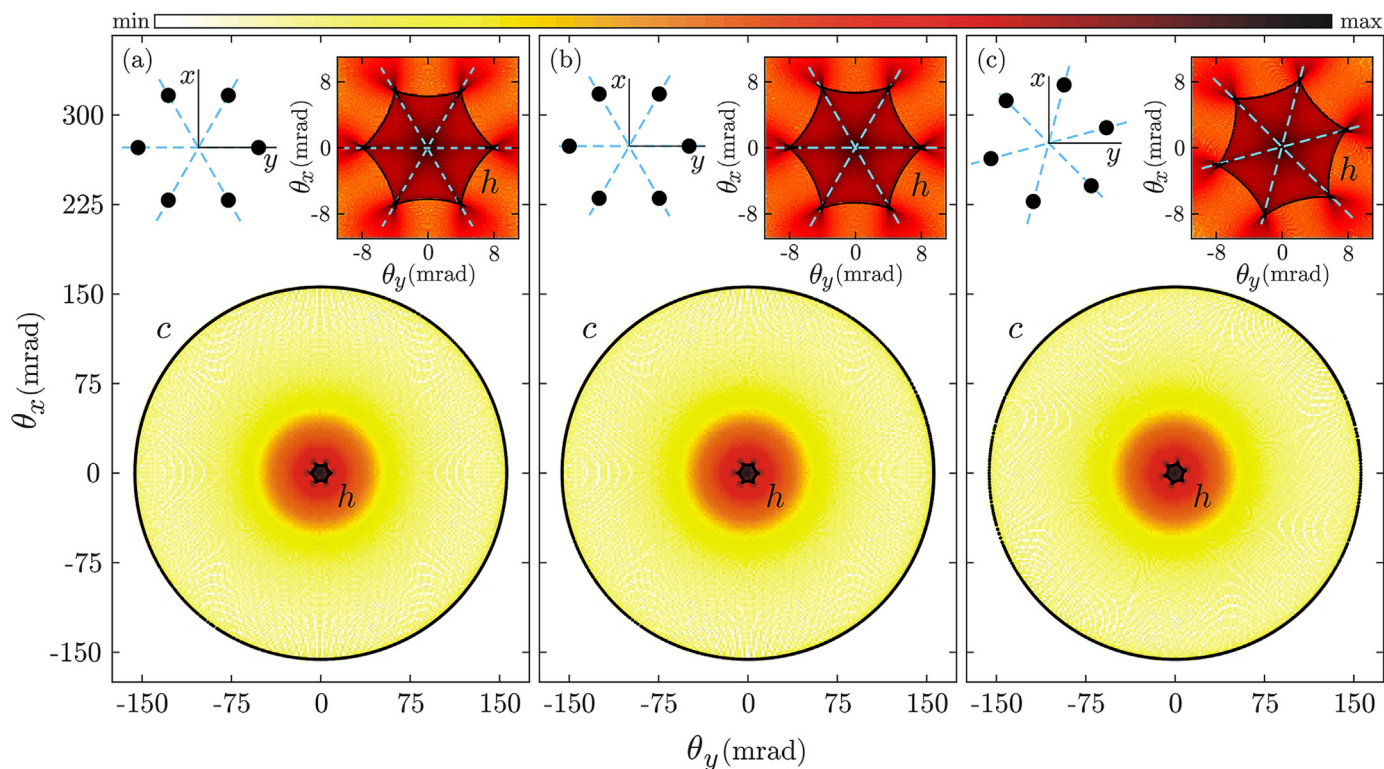|	graphene	nanoribbon
σ_x^2 (pm^2)	17.6716 ± 0.0022	18.1376 ± 0.0007
σ_y^2 (pm^2)	17.6628 ± 0.0024	35.4455 ± 0.0067
σ_z^2 (pm^2)	2619.1019 ± 1.6661	3698.1845 ± 2.6935
σ_{xy} (pm^2)	-0.0398 ± 0.0403	0.0246 ± 0.0300
σ_{xz} (pm^2)	0.3145 ± 0.1411	-0.6065 ± 0.6261
σ_{yz} (pm^2)	-0.3351 ± 0.3203	-0.2413 ± 0.6598

Fig. 3. The angular rainbow lines with corresponding angular distributions in the logarithmic scale for isotropic thermal vibrations and in the case of: (a) normal incidence; (b) sample tilted by an angle $\Theta = 0.065\pi$ rad; (c) sample additionally rotated by an angle $\Phi = 0.25\pi$ rad. Projections of the graphene hexagon on the transverse plane are shown in the corresponding upper left corners. Enlarged central parts of the distributions are shown in insets in the corresponding upper right corners. Thin dashed blue lines show directions of carbon atoms in respect to the center of the unit cell. (A colour version of this figure can be viewed online.)

upper right corners. Projections of the graphene hexagon on the transverse plane are shown in the corresponding upper left corners. It is clear that rainbow lines dominantly determine the shape of the corresponding angular distributions.

Inner rainbow lines in the Fig. 3 of hexagonal shape are labeled h. In the case of the normal incidence [see Fig. 3(a)] line h have shape of regular hexagonal with the butterfly-like joining of the hexagon sides. Rainbow line h in Fig. 3(b) is horizontally downscaled by approximately the same factor as a projection of the graphene on the transverse plane. Two horizontal butterfly-like joining of the hexagon sides are unaffected while four other are highly deformed. Analysis have shown that line h in Fig. 3(c) is deformed and rotated by the same amount as projection of the graphene on the transverse plane. All butterfly-like joining of the hexagon sides from the Fig. 3(a) are now reduced to the cusp-swallowtail combination. Thin dashed blue lines indicate directions of nearest carbon atoms in respect to the direction of the proton beam. Note that in all cases corners of the line h are directed toward carbon atoms *i.e.* it behaves as if being attracted toward carbon atoms. This figure clearly proves that rainbow line h is generated by synergetic action of carbon atoms forming graphene hexagon.

Outer rainbow patterns shown in the Fig. 3 consists of two perfectly overlapping circular lines both of them labeled c. In the case of the normal incidence the diameter of the rainbow c is $D_c = 311.98$ mrad. For sample tilted by an angle $\Theta = 0.065\pi$ rad diameter of the line c is now $D_c = 311.94$ mrad. Rainbow lines for the sample tilted by angle $\Theta = 0.065\pi$ and rotated by angle $\Phi = 0.25\pi$ rad respectively, are shown on the Fig. 3(c). New diameter of the line c is $D_c = 311.92$ mrad. Note that outer rainbow lines from Fig. 3(a), (b), and (c) practically coincide.

Figure 4(a) shows a vertical cross-section through angular distribution from the Fig. 3(a). Positions of peaks laying on the rainbow lines h and c are indicated by the arrow-lines, and are labeled by the same letters. Note the abrupt and large change of the proton yield in the vicinity of the rainbow lines. This is consequence of the change of the multiplicity of the mapping $\boldsymbol{\theta} \rightarrow \boldsymbol{b}$ characteristic for the rainbow effect, and because of it rainbow peaks are always highly asymmetrical. The base of the peak is on the dark side of the rainbow (where proton density is low) its summit is at the rainbow line, while its other end is on the light side of the rainbow (where proton density is high). Note that total variation of the proton density near rainbow h is considerably larger than near rainbow c. Interiors of the rainbow lines h and c are their bright sides, while their exteriors are rainbow dark sides. There are no scattered protons in the region beyond the rainbow line c. Therefore extent of the angular distribution is determined by the outer rainbow line c.

It is evident from the Fig. 3 that the proton distributions have hexagonal shape in the vicinity of the rainbow line h while in the region near rainbow c their shape is axially symmetric. For intermediary angles the shape of the angular distribution changes gradually form hexagonal to the circular. Note that in the vicinity of the graphene hexagon center potential is dominantly determined by contributions of the 6 atoms at the vertices of the hexagon. Consequently potential has hexagonal symmetry. Very close to any vertex graphene potential is dominated by potential of the individual atom which is axially symmetric. For intermediary distances from the carbon atom the interaction potential is dominantly determined by the contributions of its three nearest neighbors, and resulting potential has a symmetry of a triangle (see Fig. 3(a) in the Ref. [5]). Observed evolution of the angular distribution corresponds to the change of the symmetry of the graphene potential for
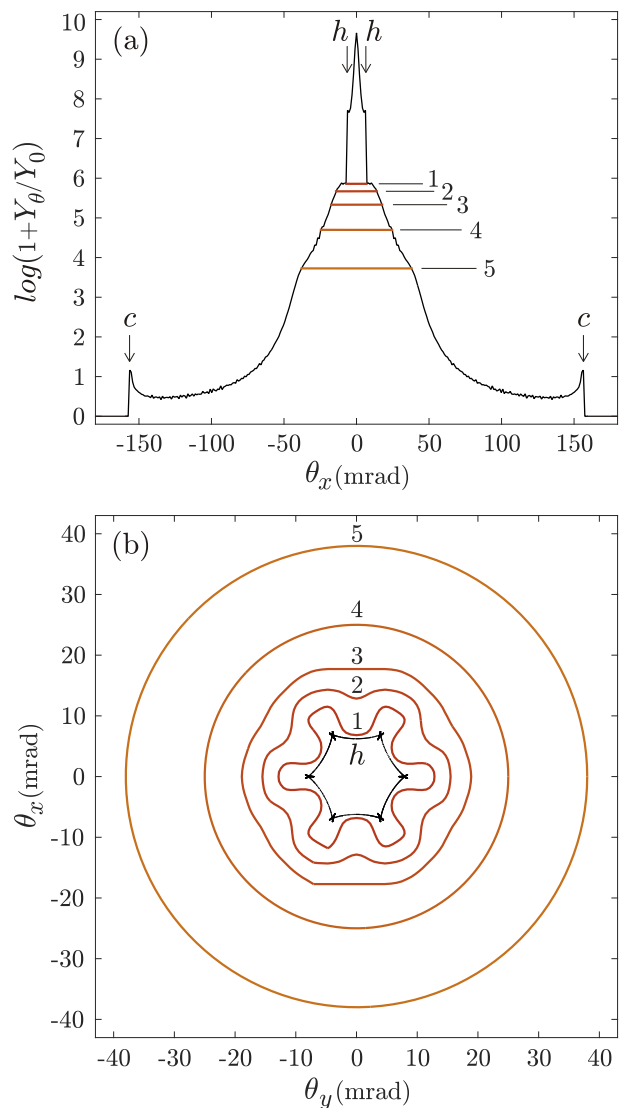
Fig. 4. (a) The vertical slice through angular distribution from Fig. 3(a) where normalization factor Y_0 is $1/mrad^2$. (b) Filtered iso-level lines of the distribution from Fig. 3(a) in the vicinity of the rainbow line h. (A colour version of this figure can be viewed online.)

horizontal lines, labeled by the same numbers. In the region of interest the angular distribution is monotonously decreasing function, without abrupt jumps characteristic for the rainbow effect. Therefore, observed transition of the shape of angular distribution from hexagonal to the circular is forced by the rainbow effect but not directly related to it.

Figure 5 shows rainbow lines together with corresponding angular distribution in the case of infinite perfect graphene sheet ($\sigma_\rho^2 = 17.67$ pm^2 and $\sigma_z^2 = 2619.10$ pm^2) for normal incidence Fig. 5(a), sample tilted by an angle $\Theta = 0.065\pi$ rad Fig. 5(b), and sample additionally rotated by an angle $\Phi = 0.25\pi$ rad Fig. 5(c). Enlarged views of the central parts of presented images and projections of the graphene hexagon on the transverse plane are also shown. This figure also confirm that rainbow lines determine the shape of the corresponding angular distributions.

Inner rainbow lines h have the same shape as corresponding lines from the Fig. 3. Comparison of the Figs. 3(a) and 5(a) reveals that for normal incidence rainbow lines h almost coincide (areas enclosed by the lines h differ by less than 0.55%). For the reoriented sample, the difference between corresponding rainbow lines in Fig. 5(b) and (c), and their counterparts in Fig. 3(b) and (c) is also small (corresponding areas enclosed by the lines h differ by less than 2.3%, and 2.7%, respectively). Note that in-plane vibration variances are almost equal ($\sigma_\rho^2 = 17.67$ and $\sigma = 17.37$ pm^2), while there is a large difference between variances of the off-plane motion ($\sigma_z^2 = 2619.10$ pm^2 and $\sigma = 17.37$ pm^2) which should be visible for tilted sample. This only means that thermal vibrations have very small influence on proton trajectories which generate inner rainbow line h.

Outer rainbow pattern for the normal incidence is shown in the Fig. 5(a). It consists of two perfectly overlapped circular lines labeled c having diameter of $D_c = 261.77$ mrad. For sample tilted by an angle $\Theta = 0.065\pi$ rad outer rainbow pattern is shown in Fig. 5(b). It consists of two overlapped elliptical lines labeled e.

Strictly speaking, tilting deforms the circular rainbow c into the "egg-shaped" curve. To explain formation of this shape let us for a moment neglect the dynamics in the longitudinal direction. In that case, momentum approximation applies, and it can be shown that resulting rainbows have shape of a perfect ellipse (see Appendix A). Therefore an interplay between dynamics in the longitudinal direction and in transverse plane is responsible for resulting distortion of an ellipse into the observed shape. However, since this distortion is small we shall refer to rainbows as elliptical.

In order to characterize the shape of the rainbows e in the simplest manner we have defined the characteristic axes of the curve as the direction running through curves centroid for which the difference between original curve and its mirror image is the smallest. We have examined all elliptical outer rainbows calculated for this study and find that they have only two characteristic axes. In the case of the perfect ellipse characteristic axes coincide with major and minor axes of an ellipse. Major and minor diameter of the rainbow line are defined as larger and smaller lengths of the cross-sections along characteristic axes.

Characteristic directions for rainbow e in Fig. 5(b) were found to point in the vertical and horizontal directions, respectively. Major and minor diameters were found to be $D_e^M = 199.93$ mrad and $D_e^m = 161.12$ mrad, respectively. The difference between diameters of overlapped rainbows [unobservable in Fig. 5(b)] was found to be smaller than 0.13 mrad and was neglected from the subsequent analysis. The centroid of the line e is displaced approximatively by vector $\Delta\theta_c = (-7.58, 0)$ mrad away form the direction of the proton beam. It should be noted that this displacement do not exists in the momentum approximation, which gives ellipse perfectly aligned with the proton beam. For the tilted sample in the transverse plane near carbon atoms proton-carbon interaction potential becomes

point moving from the center of the graphene hexagon to the carbon atom at the vertex of the hexagon. To demonstrate this fact we have analysed the iso-level lines of the distribution from the Fig. 3(a) in the region where mentioned transition happens. Figure 4(b) shows considered iso-level lines filtered by the low-pass filter to remove statistical fluctuations and reveal their overall shape more clearly. Level lines labeled 1, and 2, the closest to the rainbow line h, have shape of concave curved hexagon. They are formed by the protons of impact parameters from the area where interaction potential is hexagonal. Level lines 3, and 4 have shape of the curved convex hexagon, while the shape of the level line 4 is almost circular. Both of them are formed by protons coming from region of the impact parameter with triangular shape. There are two such regions in the graphene unit cell which are mirror image of each other. Their combined effect is the concave hexagonal shape of the mentioned level lines. The level line 5 has circular shape and is formed by the protons coming from the regions near carbon atoms where interaction potential is axially symmetric. Level values of the curves shown in the Fig. 4(b) are also shown in the Fig. 4(a) as
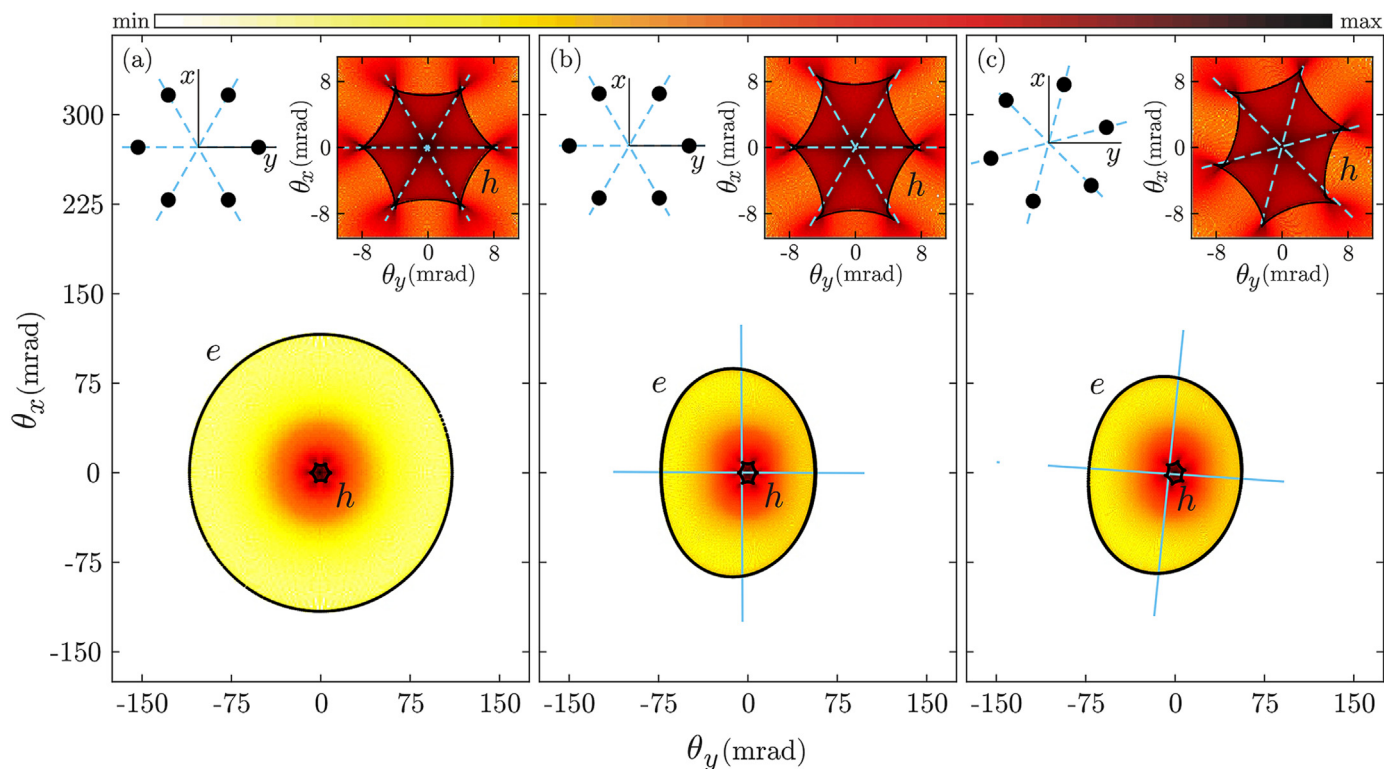
Fig. 5. The angular rainbow lines with corresponding angular distributions in the logarithmic scale for infinite perfect graphene sheet and in the case of: (a) normal incidence; (b) sample lilted by an angle $\Theta = 0.065\pi$ rad; (c) sample tilted and rotated by angles $\Theta = 0.065\pi$ rad and $\Phi = 0.25\pi$ rad, respectively. Projections of the graphene hexagon on the transverse plane are shown in the corresponding upper left corners. Enlarged central parts of the distributions are shown in insets in the corresponding upper right corners. Thin dashed blue lines show directions of carbon atoms in respect to the center of the unit cell. (A colour version of this figure can be viewed online.)

asymmetrical which results in the asymmetric scattering angles.

Outer rainbow pattern for the sample tilted and rotated by the angles $\Theta = 0.065\pi$ rad, and $\Phi = 0.25\pi$ rad is shown in the Fig. 5(c). It consists of two overlapped elliptical lines labeled e. Characteristic axes were found to point in vertical and horizontal directions, respectively. Major and minor diameters were found to be $D_e^M = 200.21$ mrad and $D_e^m = = 160.91$ mrad, respectively. Origin of the line e is shifted approximatively by an angle $\Delta\theta_c = (-7.78, -0.06)$ mrad. The difference between diameters of overlapped rainbows [also unobservable in Fig. 5(c)] was found to be smaller than 0.09 mrad and was also neglected.

Figure 6 show rainbow pattern together with corresponding angular distribution in the case of nanoribbons ($\sigma_x^2 = 18.14$ pm^2, $\sigma_y^2 = 35.45$ pm^2, $\sigma_z^2 = 3698.18$ pm^2) for normal incidence Fig. 6(a), sample tilted by an angle $\Theta = 0.065\pi$ rad Fig. 6(b), and additionally rotated by an angle $\Phi = 0.25\pi$ rad Fig. 6(c). Enlarged views of the central parts of presented images and projections of the graphene hexagon on the transverse plane are also shown. This figure also confirm that rainbow lines determine the shape of the corresponding angular distributions.

Note that inner rainbow lines h have the same shape and approximately the same size as corresponding lines in Figs. 3 and 5. The difference between sizes of the corresponding areas enclosed by the lines h from Figs. 3 and Figs. 6, respectively are less then 0.7%, 1.4%, and 2.9%, respectively. This result also confirms that inner rainbow h is practically insensitive to the thermal vibrations.

Outer rainbow pattern in the case of the normal incidence is shown in the Fig. 6(a). It consists of the two perfectly overlapped ellipses labeled e, centered at the direction of the proton beam. Characteristic directions we found to point in the horizontal and vertical directions, respectively. Major and minor diameters were

found to be $D_e^M = 231.97$ mrad and $D_e^m = 220.39$ mrad. For sample tilted by an angle $\Theta = 0.065\pi$ rad outer rainbow pattern shown in Fig. 6(b) consists of two overlapped elliptical lines labeled e. Its characteristic directions point in the horizontal and vertical directions, respectively. Major and minor diameters of line e are $D_e^M = 173.23$ mrad and $D_e^m = 129.58$ mrad. The difference between diameters of overlapped rainbows [unobservable in Fig. 6(b)] was found to be smaller than 0.15 mrad and was neglected from the subsequent analysis. Centroid of the ellipse e was found to be shifted approximatively by a vector $\Delta\theta_c = (-5.10, 0)$ mrad. For sample tilted by an angle $\Theta = 0.065\pi$ rad and rotated by an angle $\Phi = 0.25\pi$ outer rainbow patter shown in Fig. 6(c) consists of two overlapped elliptical lines labeled e. Its characteristic directions are orthogonal, and slanted by 103.55 mrad off the vertical direction. Major and minor diameters of the line e were found to be $D_e^M = 164.47$ mrad and $D_e^m = 128.14$ mrad respectively. Approximate displacement of the rainbow e was found to be $\Delta\theta_c = (-5.30, -0.80)$ mrad.

To summarize, in all analysed cases shape of the inner rainbow h reflects the structure of the sample, and is practically unaffected by the thermal vibrations. In the case of the isotropic thermal vibrations outer rainbow line have shape of a perfect circle regardless of the sample orientation. In the case of the carbon thermal motion isotropic in the graphene plane only, sample tilting transforms circular outer rainbow c for the normal incidence to elliptical line e which is unaffected by the additional rotation of the sample. In the case of the most general thermal motion, outer rainbow line always have elliptical shape. Sample tilt increase its ellipticity, while additional rotation of the sample tilts rainbow e.

Observed evolution of the outer rainbow lines with rotation angles behave in the same fashion as the normal projection of the
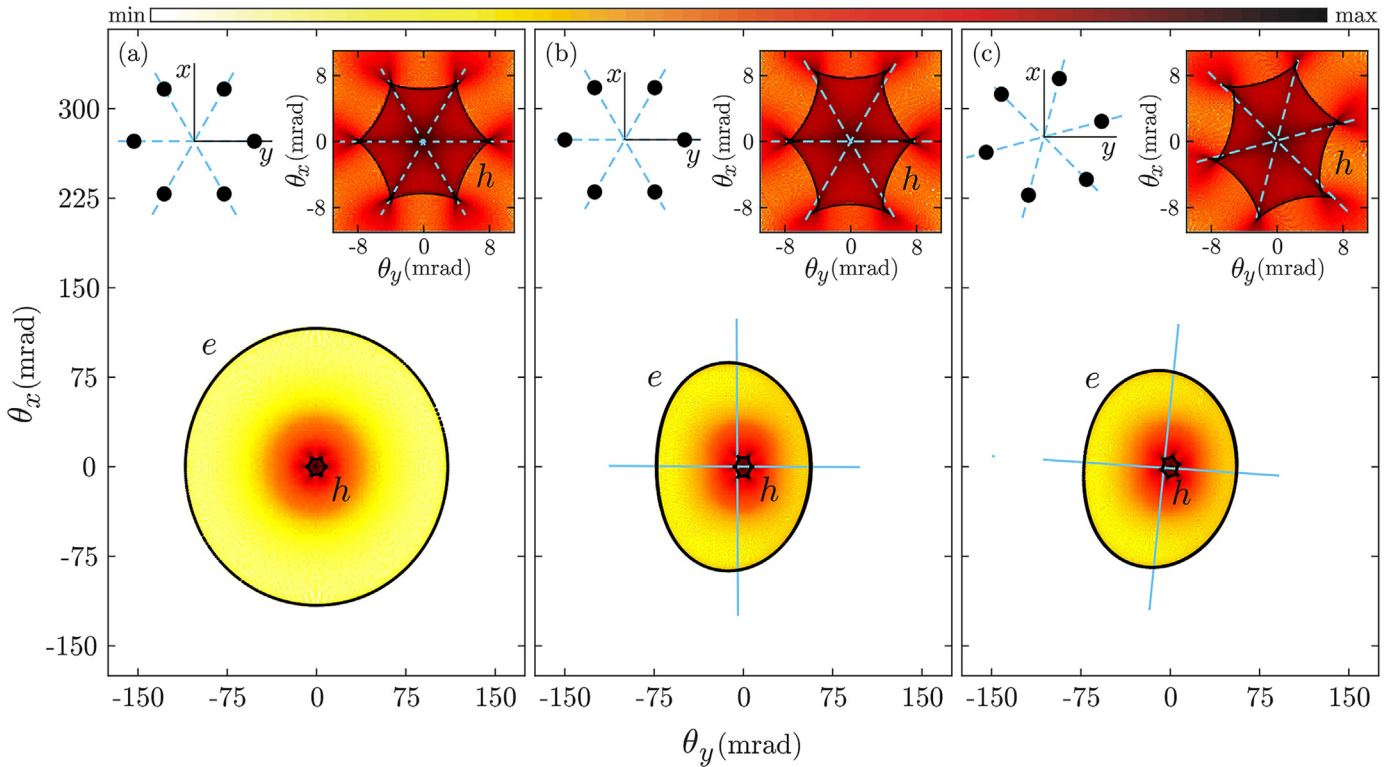
Fig. 6. The angular rainbow lines with corresponding angular distributions in the logarithmic scale for graphene nanoribbon in the case of: (a) normal incidence; (b) sample lilted by an angle $\Theta = 0.065\pi$ rad; (c) sample tilted and rotated by angles $\Theta = 0.065\pi$ rad and $\Phi = 0.25\pi$ rad, respectively. Projections of the graphene hexagon on the transverse plane are shown in the corresponding upper left corners. Enlarged central parts of the distributions are shown in insets in the corresponding upper right corners. Thin dashed blue lines show directions of carbon atoms in respect to the center of the unit cell. (A colour version of this figure can be viewed online.)

ellipsoid associated with the matrix $\Sigma^{-1} = \text{diag}(\sigma_x^{-2}, \sigma_y^{-2}, \sigma_z^{-2})$. For isotropic thermal vibrations projection of the ellipsoid $\Sigma = \sigma I$ is always a circle. In the case of infinite graphene sheet, ellipsoid $\Sigma^{-1} = \text{diag}(\sigma_\rho^{-2}, \sigma_\rho^{-2}, \sigma_z^{-2})$ have two large semi-axes σ_ρ^{-2} and the third small σ_z^{-2}. For normal incidence its projection is a large circle. For any other orientation its projection is a smaller ellipse. In the case of graphene nanoribbon matrix $\Sigma^{-1} = \text{diag}(\sigma_x^{-2}, \sigma_y^{-2}, \sigma_z^{-2})$ have two large semi-axes σ_x^{-2}, and σ_y^{-2}, and one small σ_z^{-2}. For normal incidence projection of the ellipsoid is a large ellipse. For any other orientation its projection is a smaller tilted ellipse.

3.3. Extraction of the covariance matrix from the rainbow patterns

In this section it will be shown that there is one-to-one correspondence between parameters of the outer rainbow lines and covariance matrix, which allow unambiguous extraction the covariance matrix for the outer rainbow patterns even in the general case when atoms move in fully anisotropic and correlated fashion.

We will assume that direction of the normal to the graphene sample is known in advance. Additionally we assume that matrix Σ is full, symmetric and positive definite. By suitable rotation this matrix can be transformed into the diagonal form $\overline{\Sigma} = \text{diag}(\overline{\sigma}_x^2, \overline{\sigma}_y^2, \overline{\sigma}_z^2)$ i.e it is possible to find a coordinate system in which thermal vibrations are uncorrelated. In general there are three types of rotationally nonequivalent matrix formes: the isotropic $\overline{\Sigma} = \overline{\sigma} I$, planar $\overline{\Sigma} = \text{diag}(\overline{\sigma}_\rho^2, \overline{\sigma}_\rho^2, \overline{\sigma}_z^2)$, and uncorrelated $\overline{\Sigma} = \text{diag}(\overline{\sigma}_x^2, \overline{\sigma}_y^2, \overline{\sigma}_z^2)$. This classification correspond to the number of distinct eigenvalues in the matrix spectrum. Eigenvectors of the matrix Σ define three orthogonal characteristic directions associated with corresponding eigenvalue.

Bearing in mind the evolution of the rainbow lines presented in the previous section it is relatively easy for the experimentalist to recognize the type of $\overline{\Sigma}$ he is dealing with. If covariance matrix is isotropic ($\overline{\Sigma} = \overline{\sigma} I$) then for the arbitrary orientation of the sample experimentalist would see circular rainbow. Therefore, the diameter of the rainbow D_c can only depend on the variance $\overline{\sigma}$. The curve representing dependency $D_c(\overline{\sigma})$ in Fig. 7(a) is obtained by interpolation of diameters obtained by numerical simulation for 10 equispaced $\overline{\sigma}$ values. Minimal considered value of 15.20 pm^2 correspond to thermal vibration variance at the temperature of absolute zero which was calculated according to Eq. (13). Maximal considered value was 20.6 pm^2. Square marker indicate diameter of the rainbow $D_c = 311.98$ mrad form the Fig. 3(a). Since obtained curve is monotonically decreasing "unknown" value for $\overline{\sigma}$ of the 17.37 pm^2 can be simply read from the graph.

In the case of planar matrix $\overline{\Sigma} = \text{diag}(\overline{\sigma}_\rho^2, \overline{\sigma}_\rho^2, \overline{\sigma}_z^2)$ for arbitrary sample orientation experimentalist would observe an ellipse. When proton beam is aligned with the third characteristic direction the ellipse transforms into the large circle. Note that in the reference frame attached to the proton beam major and minor axes of the ellipse always correspond to the vertical and horizontal cross-sections. Therefore, diameters of ellipses D_e^M, and D_e^m depend on $\overline{\sigma}_\rho^2, \overline{\sigma}_z^2$ and a polar angle Θ. To find two unknown eigenvalues $\overline{\sigma}_\rho^2, \overline{\sigma}_z^2$ at least two different measurements are required. For simplicity we will use the diameter of the circle D_c from Fig. 5(a) and the minor diameter of the ellipse D_e^m from Fig. 5(b). Note that this choice fixes values for the angle Θ, and produce a system of equations $D_c(\overline{\sigma}_\rho^2, \overline{\sigma}_z^2)$, $D_e^m(\overline{\sigma}_\rho^2, \overline{\sigma}_z^2)$, depending only on two unknown variances.

In principle it is possible to perform calculations for arbitrary point in the $(\overline{\sigma}_x^2, \overline{\sigma}_z^2)$ space and determine D_c and D_e^m. However, such direct evaluations are impractical. We have noticed that the
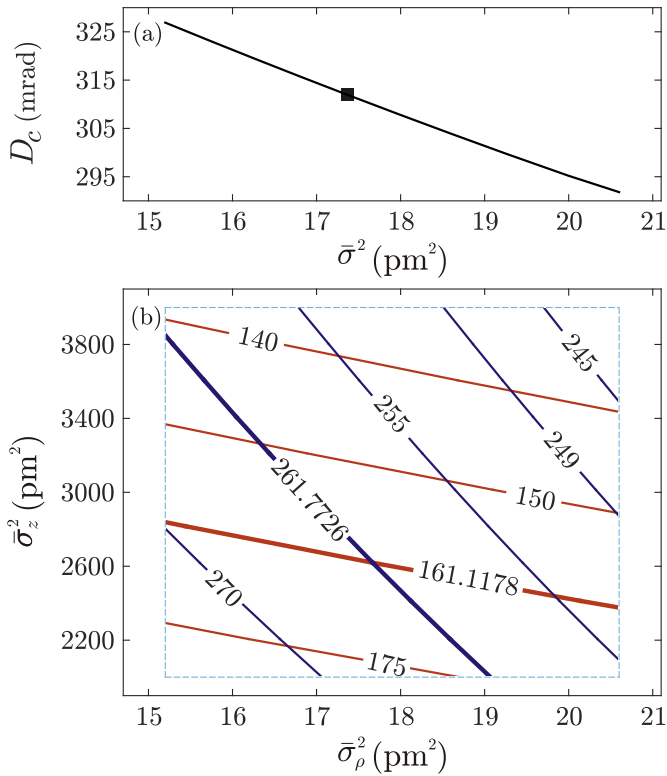
Fig. 7. (a) Dependency of the rainbow diameter D_c on the variance $\bar{\sigma}^2$, in the case of the normal incidence. Square marker indicate diameter of the rainbow c form the Fig. 3(a). (b) Blue lines represent level lines of the rainbow diameter $D_c(\bar{\sigma}_\rho, \bar{\sigma}_z)$ in the case of normal incidence. Red lines represent level lines of rainbow minor diameter $D_e^m(\bar{\sigma}_\rho, \bar{\sigma}_z)$ for the sample tilted by the angle $\Theta = 0.065\pi$ rad. Boundaries of the domain are shown by dashed blue lines. Level values are expressed in mrad. Thick blue and red lines show corresponding diameters of the rainbows c and e form the Fig. 5(a) and (b) respectively. (A colour version of this figure can be viewed online.)

dependence of the functions $D_c(\bar{\sigma}_\rho^2, \bar{\sigma}_z^2)$, $D_e^m(\bar{\sigma}_\rho^2, \bar{\sigma}_z^2)$ on $\bar{\sigma}_z^2$ is very weak in the domain $[15.2, 20.6]$ pm^2 $\times$ $[2000, 4000]$ pm^2. This fact vas be exploited to considerably reduce a number of the required calculation. Values of D_c and D_e^m were determined only on appropriately chosen grid having 81 points in the total. We have found that 2D interpolation gives desired values of the functions $D_c(\bar{\sigma}_\rho^2, \bar{\sigma}_z^2)$, $D_e^m(\bar{\sigma}_\rho^2, \bar{\sigma}_z^2)$ at arbitrary point in the domain with excellent accuracy.

Figure 7(b) show numerically obtained level lines of functions $D_c(\bar{\sigma}_\rho^2, \bar{\sigma}_z^2)$ and $D_e^m(\bar{\sigma}_\rho^2, \bar{\sigma}_z^2)$. Blue and red lines show equi-diameter level lines of the functions $D_c(\bar{\sigma}_\rho^2, \bar{\sigma}_z^2)$, and $D_e^m(\bar{\sigma}_\rho^2, \bar{\sigma}_z^2)$ respectively. Thicker contours correspond the diameters of rainbows c and e form Fig. 5(a) and (b), respectively. Note that for each level there is only one level line, and their intersections contain maximally one point. Thus, intersection of level lines corresponding to the pair $(D_c, D_e^m) = (261.77, 161.12)$ mrad contains only one point namely $(\bar{\sigma}_\rho^2, \bar{\sigma}_z^2) = (17.67, 2619.10)$ pm^2.

In the case of generic covariance matrix $\overline{\Sigma} = \text{diag}(\bar{\sigma}_x^2, \bar{\sigma}_y^2, \bar{\sigma}_z^2)$ for arbitrary sample orientation experimentalist would observe a tilted ellipse. Now diameters of an ellipse D_e^M, D_e^m, and a tilt angle Ψ are function of three variances $\bar{\sigma}_x^2, \bar{\sigma}_y^2$, $\bar{\sigma}_z^2$ and two angles Θ, and Φ. Determination of the unknown eigenvalues $\bar{\sigma}_x^2, \bar{\sigma}_y^2$, and $\bar{\sigma}_z^2$ now requires at least three different measurements. For simplicity we chose the major diameter D_e^M of the ellipse from the Fig. 6(a), the minor diameter D_e^m of ellipse form Fig. 6(b), and the major diameter D_e^M from the Fig. 6(c), relabeled D_e^M, $\mathscr{D}_e^m$ and $\mathfrak{D}_e^M$, respectively, for
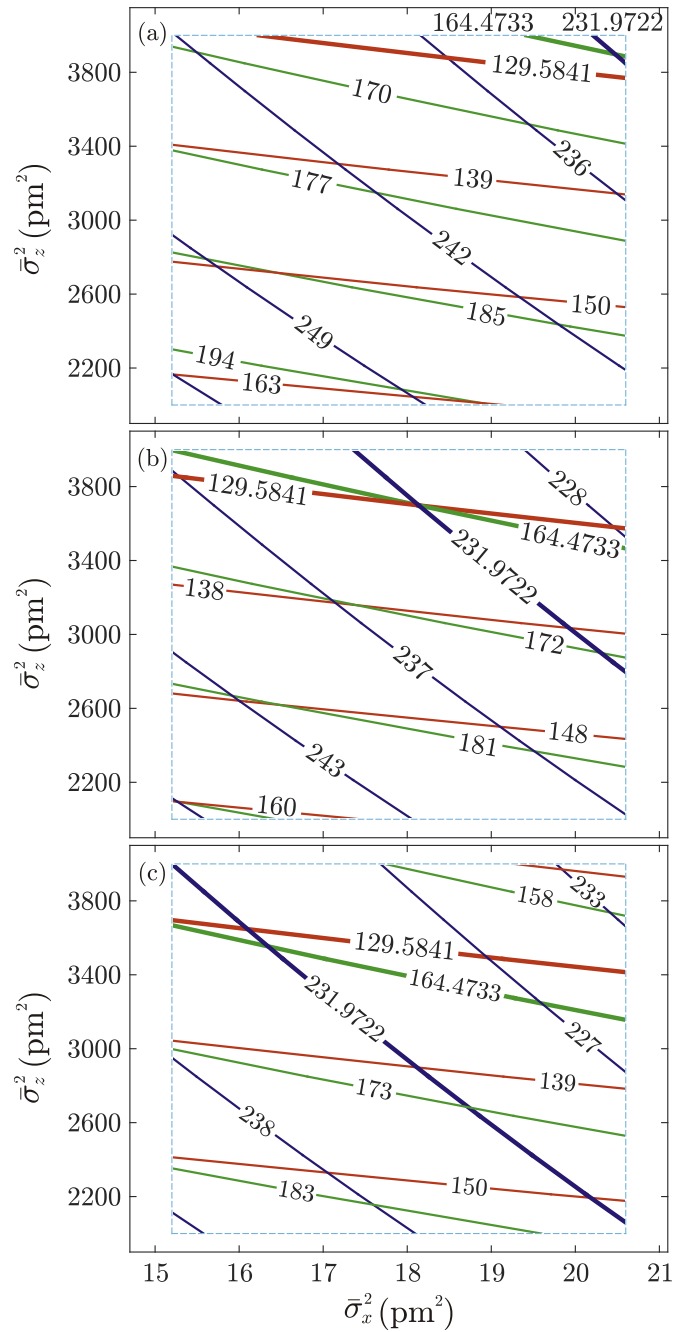

Fig. 8. The blue, red and green lines represent cross-sections through level surfaces of the rainbow diameter $D_e^M(\bar{\sigma}_x, \bar{\sigma}_y, \bar{\sigma}_z)$ in the case of normal incidence $\mathscr{D}_e^m(\bar{\sigma}_x, \bar{\sigma}_y, \bar{\sigma}_z)$ in the case of sample tilted by the angle $\Theta = 0.065\pi$, and $\mathfrak{D}_e^M(\bar{\sigma}_x, \bar{\sigma}_y, \bar{\sigma}_z)$ in the case sample additionally rotated by the angle $\Phi = 0.25\pi$, respectively, for: (a) $\bar{\sigma}_x = 30.00$ pm^2, (b) $\bar{\sigma}_x = 35.45$ pm^2, and (c) $\bar{\sigma}_x = 40.00$ pm^2. Boundaries of the domain are shown by dashed blue lines. Level values are expressed in mrad. Thicker blue and red lines show corresponding diameters of the rainbows from the Fig. 6(a), (b) and (c) respectively. (A colour version of this figure can be viewed online.)

this purpose. This choice of sample orientations produces the system of equation $D_e^M(\bar{\sigma}_x^2, \bar{\sigma}_y^2, \bar{\sigma}_z^2)$, $\mathscr{D}_e^m(\bar{\sigma}_x^2, \bar{\sigma}_y^2, \bar{\sigma}_z^2)$ and $\mathfrak{D}_e^M(\bar{\sigma}_x^2, \bar{\sigma}_y^2, \bar{\sigma}_z^2)$ depending only on the three unknown variances. For this functions set of equivalue points form surfaces in the three dimensional space which can't be represented easily on two dimensional sheet of the paper. Therefore, for simplicity Fig. 8(a), (b), and (c) show only three slices through level surfaces corresponding to the $\bar{\sigma}_y^2 = 30.00$ pm^2,

$\overline{\sigma}_y^2 = 35.45\,\text{pm}^2$, and $\overline{\sigma}_y^2 = 40.00\,\text{pm}^2$, respectively, obtained applying the same procedure described earlier. Level lines of the functions D_e^M, $\mathscr{S}_e^m$, and $\mathfrak{D}_e^M$ in the $\overline{\sigma}_x^2, \overline{\sigma}_z^2$ subspace are shown by red, green and blue lines respectively. The ticker contours correspond to the chosen values of diameters from Fig. 6(a), (b), and (c), respectively. This figure shows that for each level, in any slice there is only one level line. Intersection of arbitrary three level lines contains only one point. Therefore level lines corresponding to the triple $(D_e^M, \mathscr{S}_e^m, \mathfrak{D}_e^M) = (231.97, 129.58, 164.47)$ mrad meet only at the point $(\overline{\sigma}_x^2, \overline{\sigma}_y^2, \overline{\sigma}_z^2) = (18.14, 35.45, 3698.18)\,\text{pm}^2$ which is shown in the 8(b).

Since goniometer position and direction of the normal to the graphene are know, it is straightforward to construct the rotation matrix which will align third characteristic direction with the normal to the graphene sheet. This rotation transform matrix $\overline{\Sigma}$ into Σ which is in general full and symmetric. Therefore, it is possible to extract variances and correlation coefficients of the graphene thermal vibrations from the measurements of rainbow lines alone.

The error of the described procedure for measurement of the covariance matrix Σ have two main contributions. The first component is the systematic error related to the adopted model of the proton-carbon interaction potential which is additionally averaged in order to include effect of the thermal vibrations. Thermal averaging of the potential has been tested numerous times. It is a standard assumption used in interpretation of the X-ray or neutron scattering experiments. The choice of the appropriate proton-carbon interaction potential is more important. Earlier we have also shown that shape and the extent of the rainbow line h are very sensitive to the choice of the interaction potential [5]. In the Sec. 3.2 we have shown that inner rainbow pattern is practically insensitive to the carbon thermal vibrations. Therefore, it is in principle possible to use rainbow lines to extract the correct proton-carbon interaction potential on the similar lines as suggested in the Ref. [9]. We can safely assume that systematic error is small.

The second contribution to the error of the described procedure is experimental uncertainty of the position of the rainbow lines. Various physical processes such as: energy loss, fluctuations of the scattering angle, beam divergences influence the experimental width of the rainbow lines. It has been shown that dominant contribution to the width of the rainbow lines comes form the angular divergence of the proton beam [5]. Therefore the total error can be kept under control if one have sufficient control of the proton beam angular divergence.

4. Conclusions

In this paper we have explored in detail the relation between graphene carbon atom thermal motion and the corresponding angular rainbow pattern. Thermal effects were incorporated by averaging the proton-carbon interaction potential over the distribution of thermally induced atom displacements. The covariance matrix of the thermal vibration was modeled according the Debye model and calculated using molecular-dynamics approach. It was shown that these models cover all possible cases of the carbon atom thermal motion.

We have shown that rainbow pattern consists of two parts, the inner and outer one. The inner pattern, which gives information about graphene structure, is unperturbed by atom thermal vibrations, and the outer pattern which gives information about thermal motion of individual atoms. Is found that outer rainbow line can be modeled by an elliptical line, which behaves in a qualitatively equal manner as a normal projection od the ellipsoid associated with

matrix Σ^{-1}. At the end we have shown that rainbow pattern uniquely determine matrix Σ when atom perform fully anisotropic and correlated motion.

Results of this study are directly applicable for measurements of the ripplings of graphene and can be used for other similar layered materials. Generally speaking, this approach is applicable even when a priory assumption of the matrix Σ form is unavailable. We are convinced that possibility to obtain information about crystal structure together with information about atom thermal motion represents a significant contribution to the field. Also possible application of the method presented here would be determination of temperature dependence of the covariances matrix Σ.

Appendix A. Supplementary data

Supplementary data to this article can be found online at https://doi.org/10.1016/j.carbon.2019.01.020.

Appendix A. Momentum approximation

In this section we will construct the simple model of the outer rainbows, based on the momentum approximation. Transverse plane of the Descartes coordinate system is attached to the graphene plane. Direction of the proton beam is specified by polar angle Θ and azimuthal angle Φ.

Outer rainbows are generated by protons experiencing close collisions with carbon atoms. In this region Doyle-Turner's proton-carbon interaction potential reduces to the following form.

$$V(\boldsymbol{r}) = V_0 + \alpha \exp\left[-\frac{1}{4}\boldsymbol{r}^T \cdot \boldsymbol{\Upsilon}^{-1} \cdot \boldsymbol{r} \right], \tag{A.1}$$

where V_0 is a constant, α, and β are effective fitting parameters, $\boldsymbol{\Upsilon} = \beta\boldsymbol{I} + \frac{1}{2}\boldsymbol{\Sigma}$, $\boldsymbol{\Sigma} = \text{diag}(\sigma_x^2, \sigma_y^2, \sigma_z^2)$, and $\boldsymbol{r} = (x,y,z)$. It should be noted that potential (A.1) is accurate only in the designated area. We also assume that influence of the neighbouring atoms on the outer rainbows can be neglected. In the coordinate system attached to the proton beam the proton-carbon interaction potential is given by the Eq. (A.1) where matrix $\boldsymbol{\Sigma}$ is replaced by its rotational equivalent $\overline{\boldsymbol{\Sigma}} = \boldsymbol{R}_z(\Phi)^T\boldsymbol{R}_y(\Theta)^T \cdot \boldsymbol{\Sigma} \cdot \boldsymbol{R}_y(\Theta)\boldsymbol{R}_z(\Phi)$, $\boldsymbol{R}_z$, and $\boldsymbol{R}_y$ stand for rotational matrices around y and z axes, respectively. Scattering angles in the momentum approximation are given by the relation

$$\boldsymbol{\theta} = -\frac{1}{2E}\nabla_\rho \int V(\boldsymbol{r})\mathrm{d}z, \tag{A.2}$$

where $\boldsymbol{\theta} = (\theta_x, \theta_y)$, $\boldsymbol{\rho} = (x,y)$, $\nabla_\rho = (\partial_x, \partial_y)$, and E_k is proton kinetic energy. Expression on the right hand side of the Eq. (A.2) can be evaluated analytically, giving for the scattering law the following expression

$$\theta = -\frac{a}{4E}\boldsymbol{B}\cdot\boldsymbol{\rho}\,\exp\left[-\frac{1}{4}\boldsymbol{\rho}^T\cdot\boldsymbol{B}\cdot\boldsymbol{\rho}\right], \tag{A.3}$$

where $a = \alpha(\omega \det \boldsymbol{\Upsilon})^{-1/2}$, and $\boldsymbol{B} = \boldsymbol{\Omega} + \frac{1}{\omega}\boldsymbol{\gamma}\cdot\boldsymbol{\gamma}^T$ is the projection of the matrix

$$\boldsymbol{\Upsilon}^{-1} = \begin{bmatrix} \boldsymbol{\Omega}, & \boldsymbol{\gamma} \\ \boldsymbol{\gamma}^T, & \omega \end{bmatrix}. \tag{A.4}$$

in the x, y subspace. Scattering law (A.3) define a mapping of the impact parameter plane $\boldsymbol{\rho}$ to the scattering angle plane $\boldsymbol{\theta}$. According the Ref. [1] rainbow lines in the impact parameter plane are singularities of the Jacobian matrix $\boldsymbol{J}_\theta(\boldsymbol{\rho})$ associated with the mapping $\boldsymbol{\rho} \rightarrow \boldsymbol{\theta}$

$$\det \boldsymbol{J}_\theta(\boldsymbol{\rho}) = \det \boldsymbol{B}\frac{a^2}{4} - \det \boldsymbol{B}\frac{a^2}{4}\boldsymbol{\rho}^T\cdot\boldsymbol{B}\cdot\boldsymbol{\rho} = 0, \tag{A.5}$$

which are laying on the ellipse

$$\boldsymbol{\rho}^T\cdot\boldsymbol{B}\cdot\boldsymbol{\rho} = 1. \tag{A.6}$$

Rainbow line in the scattering angle plane is also ellipse defined by equation

$$\boldsymbol{\theta}^T\cdot\boldsymbol{B}^{-1}\cdot\boldsymbol{\theta} = \frac{a^2 e^2}{16 E_k^2} \tag{A.7}$$

where e is base of the natural logarithms. Final results have simple geometrical interpretation. It is easy to prove that ellipse $\boldsymbol{\rho}^T\cdot\boldsymbol{B}\cdot\boldsymbol{\rho} = 1$ is normal projection of the ellipsoid $\boldsymbol{r}^T\cdot\boldsymbol{\Upsilon}\cdot\boldsymbol{r} = 1$. Note that shape of the ellipse is dictated by the structure of the matrix $\overline{\boldsymbol{\Sigma}}$, since $\boldsymbol{\Upsilon} = \beta\boldsymbol{I} + \frac{1}{2}\boldsymbol{\Sigma}$ and $\beta\boldsymbol{I}$ is rotationally invariant matrix. When matrix $\overline{\boldsymbol{\Sigma}}$ have only one triplye degenerate eigenvalue, projected ellipse is actually a circle. If matrix $\overline{\boldsymbol{\Sigma}}$ have only two distinct eigenvalues, then normal projection is an ellipse in canonical form. If spectrum of the matrix $\overline{\boldsymbol{\Sigma}}$ consists of three distinct eigenvalues, then normal projection is a tilted ellipse. Similar conclusions holds for angular rainbow line, which are scaled normal projection of the ellipsoid associated with the matrix $\boldsymbol{\Upsilon}^{-1}$.

References

[1] N. Nešković, Rainbow effect in ion channeling, Phys. Rev. B 33 (1986) 6030—6035.
[2] H.F. Krause, S. Datz, P.F. Dittner, J. Gomez del Campo, P.D. Miller, C.D. Moak, N. Nešković, P.L. Pepmiller, Rainbow effect in axial ion channeling, Phys. Rev. B 33 (1986) 6036—6044.
[3] S. Petrović, L. Miletić, N. Nešković, Theory of rainbows in thin crystals: the explanation of ion channeling applied to *Ne* 10⁺ions transmitted through a <100> *Si* thin crystal, Phys. Rev. B 61 (2000) 184—189.
[4] S. Petrović, D. Borka, N. Nešković, Rainbows in transmission of high energy protons through carbon nanotubes, Eur. Phys. J. B 44 (2005) 41—45.
[5] M. Ćosić, S. Petrović, N. Nešković, The forward rainbow scattering of low energy protons by a graphene sheet, Nucl. Instrum. Methods Phys. Res. B 422 (2018) 54—62.
[6] V.M. Biryukov, Y.A. Chesnokov, V.I. Kotov, Crystal Channeling and its Application at High-Energy Accelerators, Springer, 1997.
[7] S. Bellucci, Carbon nanotubes: physics and applications, Phys. Status Solidi 2 (2005) 34—47.
[8] S. Bellucci, Nanotubes for particle channeling, radiation and electron sources, Nucl. Instrum. Methods Phys. Res. B 234 (2005) 57—77.
[9] S. Petrović, N. Nešković, M. Ćosić, M. Motapothula, M.B.H. Breese, Protonsilicon interaction potential extracted from high-resolution measurements of crystal rainbows, Nucl. Instrum. Methods Phys. Res. B 360 (2015) 23—29.
[10] D. Borka, S. Petrović, N. Nešković, Channeling star effect with bundles of carbon nanotubes, Phys. Lett. 354 (2006) 457—461.
[11] D. Borka, S. Petrović, N. Nešković, Rainbow effect in channeling of high energy protons in (10, 0) single-wall carbon nanotubes, Mater. Sci. Forum 494 (2005) 89—94.
[12] S. Petrović, I. Telečki, D. Borka, N. Nešković, Angular distributions of high energy protons channeled in long (10, 10) single-wall carbon nanotubes, Nucl.

[13] M. Ćosić, S. Petrović, S. Bellucci, Rainbow channeling of protons in very short carbon nanotubes with aligned stonewales defects, Nucl. Instrum. Methods Phys. Res. B 367 (2016) 37—45.
[14] A.A. Balandin, 2D Materials Properties and Devices, Cambridge University Press, Cambridge, 2017, pp. 90—103.
[15] P.J. van Zwol, S. Thiele, C. Berger, W.A. de Heer, J. Chevrier, Nanoscale radiative heat flow due to surface plasmons in graphene and doped silicon, Phys. Rev. Lett. 109 (2012), 264301—1—264301—5.
[16] H.O. Pierson, Handbook of Carbon, Graphite, Diamond and Fullerenes: Properties, Processing and Applications, Noyes Publications, Park Ridge, NJ, 1993.
[17] T. Nihira, T. Iwata, Temperature dependence of lattice vibrations and analysis of the specific heat of graphite, Phys. Rev. B 63 (2003), 134305—1—134305—16.
[18] L.X. Benedict, S.G. Louie, M.L. Cohen, Heat capacity of carbon nanotubes, Solid State Commun. 100 (1996) 177—180.
[19] E. Pop, V. Varshney, A.K. Roy, Thermal properties of graphene: fundamentals and applications, MRS Bull. 37 (2012) 1273—1281.
[20] N.D. Mermin, Crystalline order in two dimensions, Phys. Rev. 176 (1968) 250—254.
[21] J.C. Meyer, A.K. Geim, M.I. Katsnelson, K.S. Novoselov, T.J. Booth, S. Roth, The structure of suspended graphene sheets, Nature 446 (2007) 60—63.
[22] A. Fasolino, J.H. Los, M.I. Katsnelson, Intrinsic ripples in graphene, Nat. Mater. 6 (2007) 858—861.
[23] A. OHare, F.V. Kusmartsev, K.I. Kugel, A stable "flat" form of two-dimensional crystals: could graphene, silicene, germanene be minigap semiconductors? Nano Lett. 12 (2012) 1045—1052.
[24] P. Doyl, P. Turner, Relativistic hartree-foek x-ray and electron scattering factors, Acta Crystallogr. A24 (1968) 390—397.
[25] D.S. Gemmell, Channeling and related effects in the motion of charged particles through crystals, Rev. Mod. Phys. 46 (1974) 129—227.
[26] J. Lindhard, Influence of crystal lattice on motion of energetic charged particles, Mat. Fys. Medd . Dan. Vid . Selsk 34 (1965) 1—65.
[27] B.V. Gnedenko, A.N. Kolmogorov, Limit Distributions for Sums of Independent Random Variables, Addison-Wesley, Reading, Massachusetts, 1968.
[28] A.C. Rencher, Methods of Multivariate Analysis, John Wiley and Sons, inc., 2002.
[29] E. Gruber, R.A. Wilhelm, R. Pétuya, V. Smejkal, R. Kozubek, A. Hierzenberger, B. Bayer, I. Aldazabal, A.K. Kazansky, F. Libisch, A.V. Krasheninnikov, M. Schleberger, S. Facsko, A.G. Borisov, A. Arnau, F. Aumayr, Ultrafast electronic response of graphene to a strong and localized electric field, Nat. Commun. 7 (2016) 1—7.
[30] M.B.H. Breese, D.N. Jamieson, P.J.C. King, Materials Analysis Using a Nuclear Microprobe, Wiley, New York, USA, 1996.
[31] D. Jalabert, Real space structural analysis using 3d meis spectra from a toroidal electrostatic analyzer with 2d detector, Nucl. Instrum. Methods Phys. Res. B 270 (2012) 19—22.
[32] R. Tromp, M. Copel, M. Reuter, M.H. von Hoegen, J. Speidell, R. Koudijs, A new two dimensional particle detector for a toroidal electrostatic analyzer, Rev. Sci. Instrum. 62 (1991) 2679—2683.
[33] R. Tromp, H. Kersten, E. Granneman, F. Saris, A new uhv system for channeling/blocking analysis of solid surfaces and interfaces, Nucl. Instrum. Methods Phys. Res. B 4 (1984) 155—166.
[34] R. Smeenk, H.K.R.M. Tromp, A. Boerboom, F. Saris, Angle resolved detection of charged particles with a novel type toroidal electrostatic analyser, Nucl. Instrum. Methods Phys. Res. 195 (1982) 581—586.
[35] E. Gruber, R.A. Wilhelm, R. Pétuya, V. Smejkal, R. Kozubek, A. Hierzenberger, B. Bayer, I. Aldazabal, A.K. Kazansky, F. Libisch, A.V. Krasheninnikov, M. Schleberger, S. Facsko, A.G. Borisov, A. Arnau, F. Aumayr, Ultrafast electronic response of graphene to a strong and localized electric field, Nat. Commun. 7 (2016) 1—7 (Supplementary material).
[36] S. Zhao, W. Kang, J. Xue, X. Zhang, P. Zhang, Comparison of electronic energy loss in graphene and BN sheet by means of time-dependent density functional theory, J. Phys. Condens. Matter 27 (2015) 1—6.
[37] A.V. Krasheninnikov, Y. Miyamoto, D. Tománek, Role of electronic excitations in ion collisions with carbon nanostructures, Phys. Rev. Lett. 99 (2007), 016104—1—016104—4.
[38] S. Mathew, T.K. Chan, D. Zhan, K. Gopinadhan, A.R. Barman, M.B.H. Breese, Ion and electron irradiation-induced effects in nanostructured materials, J. Appl. Phys., Appl. Phys. Rev. 110 (2011), 084309—1—084309—4.
[39] A.V. Krasheninnikov, K. Nordlund, Ion and electron irradiation-induced effects in nanostructured materials, J. Appl. Phys. 107 (2010), 071301—1—071301—70.
[40] Y. Shunin, S. Bellucci, A. Gruodis, T. Lobanova-Shunina, Nonregular Nanosystems, Springer, 2018.
[41] M. Schleberger, J. Kotakoski, 2d material science: defect engineering by particle irradiation, Materials 11 (2018) 1—29.
[42] O. Lehtinen, J. Kotakoski, A.V. Krasheninnikov, A. Tolvanen, K. Nordlund, J. Keinonen, Effects of ion bombardment on a two-dimensional target: atomistic simulations of graphene irradiation, Phys. Rev. B 81 (2010), 153401—1—153401—4.
[43] B.R. Appleton, C. Erginsoy, W.M. Gibson, Channeling effects in the energy loss of 3-11-Mev protons in silicon and germanium single crystals, Phys. Rev. 161 (1967) 330—349.
[44] X. Artru, S.P. Fomin, N.F. Shul'ga, K.A. Ispirian, N.K. Zhevago, Carbon nanotubes

and fullerites in high-energy and X-ray physics, Phys. Rep. 412 (2005) 89—189.

[45] S. Plimpton, Fast parallel algorithms for short-range molecular dynamics, J. Comput. Phys. 117 (1995) 1—19. http://lammps.sandia.gov.

[46] S.J. Stuart, A reactive potential for hydrocarbons with intermolecular interactions, J. Chem. Phys. 112 (2000) 6472—6486.

[47] B.T. Kelly, The thermal vibration amplitudes of carbon atoms in the graphite lattice parallel to the *c*-axis, J. Nucl. Mater. 24 (1967) 201—214.

[48] P.L. Doussal, L. Radzihovsky, Self-consistent theory of polymerized membranes, Phys. Rev. Lett. 69 (1992) 1209—1212.

[49] C.S. Allen, E. Liberti, J.S. Kim, Q. Xu, Y. Fan, K. He, A.W. Robertson, H.W. Zandbergen, J.H. Warner, A.I. Kirkland, Temperature dependence of atomic vibrations in mono-layer graphene, Phys. Rev. B 118 (2015), 074302—1—074302—7.